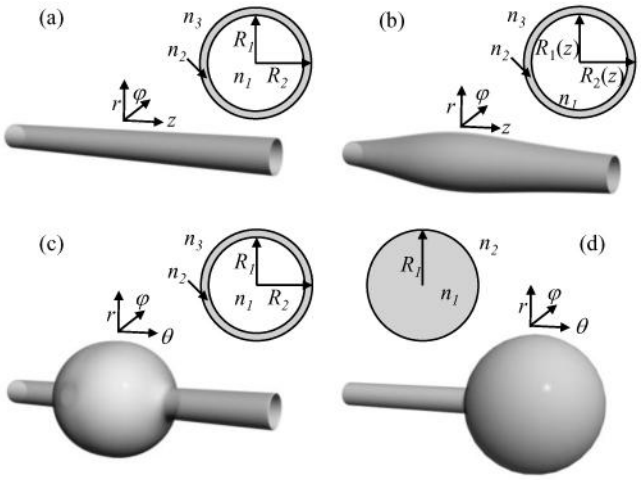

Fig. 1. Schematic of different ring resonators under study. (a) Cylindrical OFRR in cylindrical coordinates (r, θ and z with the origin at the arbitrary location on z axis). (b) Microbottle OFRR in cylindrical coordinates (r, θ and z with the origin at the bottle center). (c) Microbubble OFRR in spherical coordinates (r, θ and φ with the origin at the bubble center). (d) Solid microsphere in spherical coordinates (r, θ and φ with the origin at the sphere center).

OFRR is essentially a 2-dimentional ring resonator without any confinement along the axial direction where the other three structures provide 3-dimensional confinement. In this study, we focus on the microbottle OFRR and microbubble OFRR, whose WGMs are analyzed separately.

For the microbottle OFRR, we use the adiabatic invariants method [9, 10]. As shown in Fig. 1(b), we assume that the profile of the microbottle radius along the z direction, $R(z)$, can be described as:

$$R(z) = R_0 / \sqrt{1+(\Delta k z)^2}, \tag{1}$$

where Δk is a parameter to describe the curvature of the profile. When $(\Delta kz)^2<0.05$ (or $\Delta k<0.22$ assuming the field extension in the z direction is 1 μm) the adiabatic approximation is applicable and the field distribution $E(r, \varphi, z)$ can be separated as $E=E_r(r, z)E_\varphi(\varphi)E_z(z)$. $E_\varphi(\varphi)$ can be solved as $E_\varphi(\varphi)=\exp(im\varphi)$ and $E_r(r, z)$ can be written as [11, 12]:

$$E_r = \begin{cases} AJ_m\left(k_\varphi^{(m,l)} n_1 r\right), & r \le R_1(z) \\ BJ_m\left(k_\varphi^{(m,l)} n_2 r\right) + CH_m^{(1)}\left(k_\varphi^{(m,l)} n_2 r\right), & R_1(z) < r \le R_2(z) \\ DH_m^{(1)}\left(k_\varphi^{(m,l)} n_3 r\right), & r > R_2(z) \end{cases} \tag{2}$$

where J_m and $H_m^{(1)}$ are the mth Bessel function and mth Hankel function of the first kind, respectively. $k_\varphi^{(m,l)}$ is the amplitude of the resonant wave vector component in φ direction labeled by the azimuthal index m and the radial index l.

In the z direction, the equation for E_z is the same as the harmonic oscillator problem and the corresponding solution can be expressed as [10]:

$$E_z = E_0 H_q\left(\sqrt{\frac{m\Delta k}{R_0}} z\right) \exp\left(-\frac{m\Delta k}{2R_0} z^2\right), \tag{3}$$

where H_q is the qth Hermite polynomial. The relevant resonant wave vector component in the z direction is $k_z=[m^2/R_0^2+(2q+1)m\Delta k/R_0]^{1/2}$ and the total wave vector is $k=(k_\varphi^2+k_z^2)^{1/2}$. Note

#134450- $15.00USD Received1 Sep2010;revised16 Oct 2010;accepted22 Oct 2010;published16 Nov 2010
(C) 2010OSA

that when Δk=0, the microbottle OFRR is the same as the cylindrical OFRR in Fig. 1(a), which can be described by Eq. (2).

The electric field distribution of the microbubble OFRR, $E(r, \theta, \varphi)$, can be separated into $E_r(r)Y_l^m(\theta, \varphi)$, where Y_l^m is the spherical harmonics of the lth degree and the mth order. E_r can be written as [11]:

$$E_r = \begin{cases} Aj_m\left(k^{(m,l)}n_1 r\right), & r \le R_1 \\ Bj_m\left(k^{(m,l)}n_2 r\right) + Ch_m^{(1)}\left(k_\varphi^{(m,l)}n_2 r\right), & R_1 < r \le R_2 \\ Dh_m^{(1)}\left(k^{(m,l)}n_3 r\right), & r > R_2 \end{cases}, \quad (4)$$

where j_m and h_m are the mth order spherical Bessel function and the mth order spherical Hankel function of the first kind. Note that when n_1=n_2 in Fig. 1(c), the microbubble OFRR becomes a solid microsphere. E_r can be simplified as:

$$E_r = \begin{cases} Aj_m\left(k^{(m,l)}n_1 r\right), & r \le R_1 \\ Bh_m^{(1)}\left(k^{(m,l)}n_2 r\right), & r > R_1 \end{cases}, \quad (5)$$

In order to compare the field distribution form different structures, we also introduce the normalization condition $\int |E_r|^2 dr = 1$ and $\int |E_z|^2 dz = 1$ for all modes, where the unit of r and z is chosen to be μm.

The resonant wave vectors for all three structures (microbottle, microbubble, and solid microsphere) are numerically solved by home-made programs based on the Mie scattering theory [11].

In the presence of a nanoparticle on the ring resonator surface, the resonant wavelength shifts, which can be numerically calculated by [13, 14]:

$$\frac{\Delta\lambda}{\lambda} = \frac{\int_{particle}\left(n_p{}^2 - n^2\right)|E|^2 dV}{2\int n^2 |E|^2 dV} \quad (6)$$

where n_p and n are the refractive indices of the nanoparticle and the medium and n is usually a function of space coordinates. The integration in numerator is taken within the nanoparticle and the integration in denominator is calculated in the whole space. For simplicity, in this work only the modes with the electric field parallel to the surface are studied. The other modes with the magnetic field parallel to the surface will generate slightly better improvement in the sensitivity (approximately 25% increase in $\Delta\lambda/\lambda$) due to the electric field discontinuity at the interfaces.

3. Results and discussion

The relation between the radial distribution of the electric field of the 3rd order mode and the wall thickness is studied in Fig. 2 for the microbottle OFRR [Fig. 2(a), (b) and (c)] and microbubble OFRR [Fig. 2(d), (e) and (f)], respectively. The core of the OFRR is filled with water and the outside is air. For microbottle, the field is plotted at z=0. We choose the 3rd order mode because it can be experimentally realized based on our previous studies [6].

In Fig. 2(a) and (d), the wall thickness is 2.5 μm and the most part of the electric field resides inside the wall. According to Eq. (6), the sensitivity for surface mass detection is proportional to the field strength near the surface. Therefore, when the field at the water-glass interface is only a tail of an exponential decay, the sensitivity is low. In Fig. 2(b) and (e), the wall thickness is reduced to 1.6 μm and the first electric field peak emerges near the water-

#134450 - $15.00 USD Received 1 Sep 2010; revised 16 Oct 2010; accepted 22 Oct 2010; published 16 Nov 2010
(C) 2010 OSA

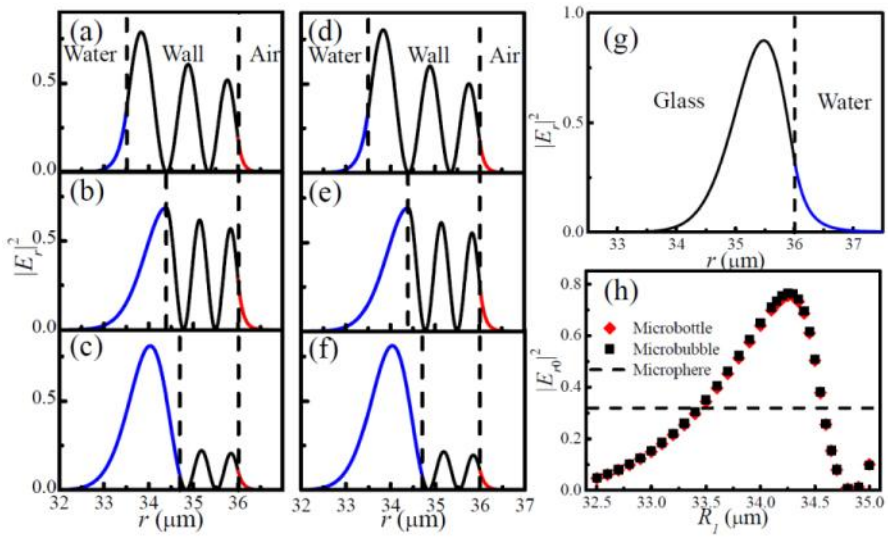

Fig. 2. The electric field distribution of the 3rd order mode in the radial direction with different wall thicknesses for the microbottle (a-c) and the microbubble (d-f). In all case, R_2=36 mm, n_1=1.33, n_2=1.45, n_3=1, m=288 for the microbottle, l=288 for the microbubble. (a) R_1=33.5 μm, λ=1022.543860 nm. (b) R_1=34.4 μm, λ=979.4255256 nm. (c) R_1=34.7 μm, λ=969.5206896 nm. (d) R_1=33.5 μm, λ=1020.959929 nm. (e) R_1=34.4 μm, λ=977.9460628 nm. (f) R_1=34.7 μm, λ=967.9444502 nm. (g) Field distribution of the 1st order mode of a microsphere in the radial direction. R_1=36 μm, n_1=1.45, n_2=1.33, l=288, λ=1040.227437 nm. (h) $|E_{r0}|^2$ vs. R_1. Dashed line represents $|E_{r0}|^2$ of the microsphere in (g).

glass interface, which increases the sensitivity for surface mass or surface adsorption detection. When the wall thickness further decreases to 1.3 μm, as shown in Fig. 2(c) and (f), the first peak of the field is pushed into the core and the surface mass sensitivity deteriorates. For comparison, the electric field of a microsphere with a radius of 36 μm surrounded with water is also drawn in Fig. 2(g). Due to the light confinement of the mode, the field peak never reaches the water-glass interface.

In Fig. 2(h), $|E_{r0}|^2$ is plotted as a function of R_1 for the microbottle and microbubble where E_{r0} is the electric field amplitude at the water-glass interface. Although the mathematical field expressions of the microbottle and microbubble are different, their $|E_{r0}|^2$ curves are virtually the same. There is a maximum value for both curves, which represents the best wall thickness for surface mass detection. The curve near the maximum changes slowly, suggesting that the requirement for the optimal wall thickness is not quite critical. In comparison with the microsphere of the same size, the microbottle and microbubble have twice as large $|E_{r0}|^2$ when the wall thickness is between 1.5 μm to 2 μm, showing the advantage of the OFRR based structures in surface mass detection. Practically, this wall thickness and the related tolerance are experimentally obtainable [6, 8, 15].

The electric field distribution along the capillary axis (*i.e.*, the z direction for the microbottle and the θ direction for the microbubble and microsphere) are also investigated. In Fig. 3(a), the field distributions of the 0th order mode in Eq. (3) for the microbottle with different Δk is shown and compared with that of the microbubble. The inset shows the actual geometries for those structures. It is clear that the large curvature can efficiently decrease the field extension and confine the light in the central region of the microbottle. We define E_{z0} as the field amplitude at z=0 (in the subsequent studies, we assume that the nanoparticle is always attached to the equator). $|E_{z0}|^2$ as a function of Δk is plotted in Fig. 3(b) and is compared with that for the microbubble. Note that at the point that $(R_0\Delta k)$=1, the microbottle becomes the microbubble and has the same field intensity, suggesting that our original adiabatic approximation to describe the microbottle is applicable and compatible with the accurate solution. When $(R_0\Delta k)$>1, $|E_{z0}|^2$ for the microbottle is larger than that for spherical

#134450 - $15.00 USD Received 1 Sep 2010; revised 16 Oct 2010; accepted 22 Oct 2010; published 16 Nov 2010
(C) 2010 OSA

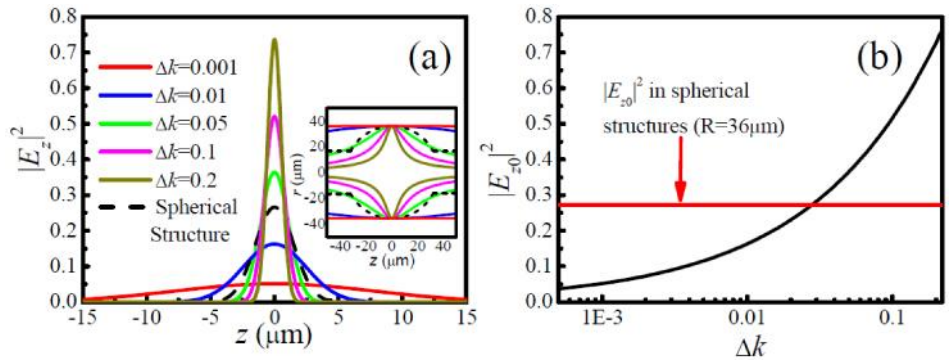

Fig. 3. (a) The normalized 0th order mode field distribution of the microbottle and microsphere along the capillary with different Δk. For the microbottle, m=288, R_0=36 μm. For the microsphere, l=288, R_1=36 μm. Inset is their actual geometries. (b) The relation between $|E_{z0}|^2$ and Δk. z=0.

structures. Therefore, in this region, the microbottle has the better sensing performance.

After the 3-dimensional electric field distribution is computed, the fractional resonant wavelength shift $\Delta\lambda/\lambda$ caused by a single nanoparticle in water is numerically calculated using Eq. (6) and the results are shown in Fig. 4. In order to obtain the maximum shift, the location of the nanoparticle is assumed to be at the equator and is at the inner surface of the OFRR based structures (or at the outer surface of the microsphere). Note that when the nanoparticle location is off the equator, the corresponding shift can be deduced by comparing the local field intensity to the peak value in Fig. 3(a).

In Fig. 4(a), $\Delta\lambda/\lambda$ for different R_1 is plotted while R_2 and the nanoparticle radius, R_p, are fixed at 36 μm and 50 nm, respectively. Polystyrene beads (n_p=1.59) are chosen as a model system to simulate viral particles [3, 4, 18]. As expected, there is a maximum shift when the wall thickness is around 1.6 μm for both microbottle and microbubble. Under this wall thickness, the electric field peak is near the water-glass interface. Also we can see that the structure with a bigger Δk has a larger shift due to the light confinement in the z direction. In Fig. 4(b), the maximum shift vs. the nanoparticle radius is plotted for different structures. The change of $\Delta\lambda/\lambda$ is basically proportional to the R_p^3, which is identical to the previously reported linear relationship between $\Delta\lambda/\lambda$ and the nanoparticle volume [3, 14]. The smallest detectable nanoparticle radius is related to the smallest detectable $\Delta\lambda/\lambda$. Practically, by controlling the instability of the light source, mechanical vibration, thermo fluctuation, and noise from the photodetector, $\Delta\lambda/\lambda$ of 10^{-8} can be achieved as demonstrated in Ref [3, 6]. Under this detection limit, we arrive at the smallest detectable nanoparticle radius of approximately 17 nm for the curve of Δk=0.2.

The dependence of the sensitivity on Δk is studied by calculating the maximum shift caused by a single nanoparticle with 50 nm in radius for different Δk. As shown in Fig. 4(c), the wavelength $(\Delta\lambda/\lambda)_{max}$-$\Delta k$ curve exceeds the microsphere value when Δk is about 0.003 and intersects with the microbubble value at Δk=0.028 where the shape of the microbottle is equivalent to microbubble. Note that in the simulation, there is no boundary for the curvature of the microbottle profile, which can increase indefinitely by continuously increasing Δk. But considering the adaptive range of adiabatic invariant assumption and fabrication limitations, we predict approximately 10 times enhancement by comparing a large Δk microbottle (Δk=0.2) with a microsphere.

Figure 4(d) plots the linear relationship between the nanoparticle size and the best wall thickness, which is related to the maximum wavelength shift. The slope of this curve is virtually unity, which may result from the fact that the peak of the electric field needs to be at the center of the nanoparticle to obtain the maximum field overlap. Note that the needed change in the best wall thickness is almost negligible when the nanoparticle radius varies less than 100 nm. As a result, in actual applications, one thickness may be sufficient to detect

#134450 - $15.00 USD Received 1 Sep 2010; revised 16 Oct 2010; accepted 22 Oct 2010; published 16 Nov 2010
(C) 2010 OSA

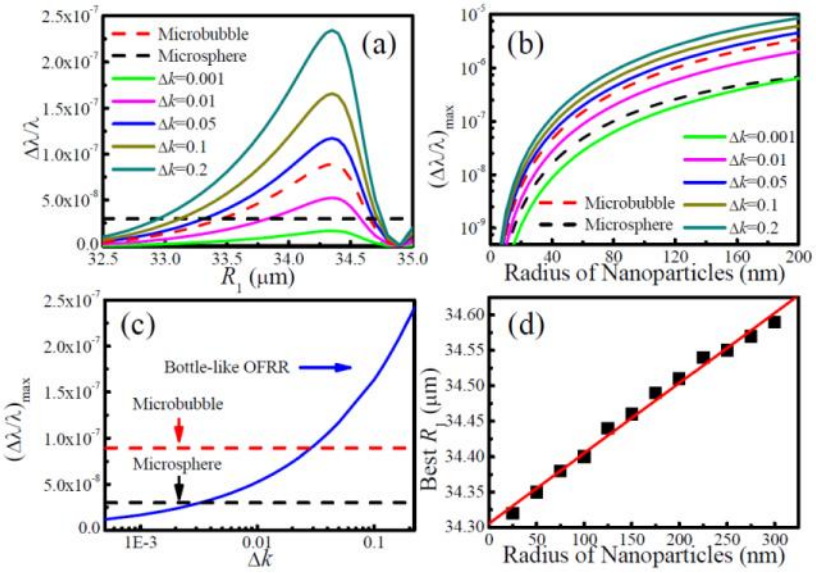

Fig. 4. Results of single nanoparticle detection in water. The modes with the 3rd order in the r direction and the 0th order in the z direction are used. For the microbottle and microbubble, R_2=36 μm, m=288, l=288, n_1=1.33, n_2=1.45, n_3=1. For the microsphere, R_1=36 μm, m=288, l=288, n_1=1.45, n_2=1.33. The nanoparticle is located at the equator and at the inner surface of the OFRR based structures or at the outer surface of the microsphere. n_p=1.59. (a) Normalized wavelength shift caused by a single nanoparticle as a function of R_1. Wavelength shift from the microsphere is also shown for comparison. Nanoparticle radius is 50 nm. (b) The maximum wavelength shift vs. the nanoparticle radius for the microbottle with different Δk, microbubble, and microsphere. (c) The wavelength shift from the microbottle as a function of Δk. (d) The best wall thickness that gives the largest spectral shift as a function of the nanoparticle radius.

nanoparticles whose radii are in the range of 100 nm.

Finally, the detection of single nanoparticle in air is also studied. Here we choose the microbubble as a representative structure. The typical electric field distribution of the 3rd order mode in the r direction is shown in Fig. 5(a). Because the capillary is filled with air (n=1), the refractive indices inside and outside the capillary are the same. Consequently, the peak of the field intensity will always be inside the wall. The Q factor related to the radiation loss of the mode with the 3rd order in the r direction and the 0th order in the θ direction is also calculated for different wall thicknesses and is shown in Fig. 5(b). Unlike the nanoparticle detection in water, in which the radiation loss is low and optical absorption of water limits the Q, the Q for the nanoparticle detection in air can be drastically degraded due to the radiation loss, which may reduce the wavelength spectral resolution and deteriorate the detection limit [13].

In Fig. 5(c), $\Delta\lambda/\lambda$ is plotted as a function of R_1 and compared with that of the microsphere. $\Delta\lambda/\lambda$ increases when the fraction of light in the air core increases. Considering Fig. 5(b) and (c) in which the sensitivity is increased at the expense of the Q factor, a trade-off wall thickness is chosen to be around 1 μm where the Q factor is still about 10^{10} and the shift is more than 10 times larger than that of the microsphere. In Fig. 5(d), $\Delta\lambda/\lambda$ for different nanoparticle radii is plotted for a microbubble with a 1-μm thick wall. The smallest detectable nanoparticle radius is also about 20 nm and the $\Delta\lambda/\lambda$ is 10 times larger than that of a microsphere across a wide range of nanoparticle radii.

4. Conclusion

In the summary, the single nanoparticle detection capability of 3-dimensional confined OFRRs is studied analytically and is compared with microsphere biosensors. In the radial direction, the electric field at the inner surface can be optimized by choosing the right wall

#134450 - $15.00 USD Received 1 Sep 2010; revised 16 Oct 2010; accepted 22 Oct 2010; published 16 Nov 2010
(C) 2010 OSA

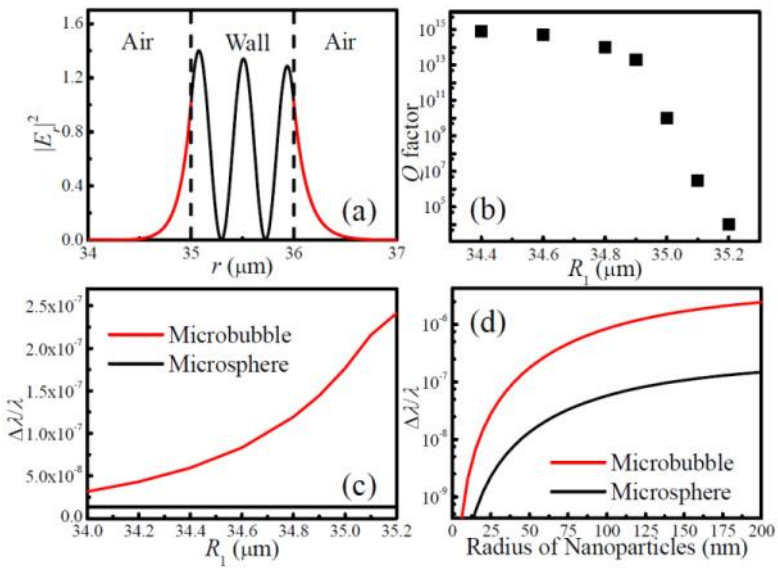

Fig. 5. Results of single nanoparticle detection in air. R_2=36 μm, n_1=1, n_2=1.45, n_3=1, m=288, l=288. (a) Field distribution of the 3rd order mode of the microbubble. R_1=35 μm, λ=784.0225833 nm. (b) Q factor of the 3rd order mode of the microbubble as a function of the inner radius. (c) Fractional wavelength shift as a function of the inner radius. Shift from a solid microsphere is also plotted for comparison. R_p=50 nm, n_p=1.59 and the single nanoparticle is located at the equator and at the inner surface of the microbubble (or at the outer surface of the microsphere). (d) Fractional wavelength shift for the microbubble and for the microsphere with different nanoparticle radii. The wall thickness of the microbubble is 1 μm.

thickness. Along the long axis, the electric field can be efficiently confined by the curvature. Both effects significantly increase the sensitivity of the OFRR for single nanoparticle detection. It is found that the sensitivity is enhanced about 10 times, as compared to that of a solid microsphere biosensor in Ref [3], and that the smallest detectable nanoparticle is estimated to be less than 20 nm in radius (assuming $\Delta\lambda/\lambda$ of 10^{-8} spectral resolution). The extension of the detection capability to smaller nanoparticle sizes enables the detection of more types of important and lethal viruses (such as SARS virus and dengue virus with radii below 50 nm) [16, 17]. Very recently, $\Delta\lambda/\lambda$ of 10^{-9} is achieved on a solid microsphere using the frequency-doubling technology via a PPLN [18]. The corresponding smallest detectable nanoparticle is reduced to 20 nm in radius [18]. Applying such a high spectral resolution technology to the OFRR should enable the detection of a nanoparticle of only approximately 7 nm in radius (see Fig. 4(b) and 5(d)). Similarly, detection of a single molecule (such as proteins whose size is around 5 nm in radius), which is the "holy grail" in label-free sensing, may even become possible. The high sensitivity for nanoparticle detection presented in this paper and for the detection of smaller molecules studied earlier [6], and the naturally integrated microfluidics make the OFRR a very promising sensing platform for detection of various sizes of bio/chemical species in liquid and in air.

Acknowledgments

This work is supported by the Wallace H. Coulter Foundation Early Career Award. H.L. is supported by China Scholarship Council (No. 2009610120) and by the University of Michigan.

#134450 - $15.00 USD Received 1 Sep 2010; revised 16 Oct 2010; accepted 22 Oct 2010; published 16 Nov 2010
(C) 2010 OSA